**ORIGINAL PAPER**

# Understanding the electrochemical behavior of bulk-synthesized MgZn$_2$ intermetallic compound in aqueous NaCl solutions as a function of pH

Alexander I. Ikeuba [1,2,3,4] · Fujun Kou [5] · Haowei Duan [5] · Bo Zhang [1,2] · Jianqiu Wang [2] · En-Hou Han [2] · Wei Ke [2]

## Abstract

The electrochemical behavior of a bulk-synthesized MgZn$_2$ intermetallic compound in aerated 0.1 M NaCl solutions has been studied as a function of pH and applied potential using polarization techniques, electrochemical impedance spectroscopy (EIS), X-ray photoelectron spectroscopy (XPS), and focused ion beam-transmission electron microscopy (FIB-TEM). The anodic activity of MgZn$_2$ is seen to decrease with an increase in pH value. Polarization tests reveal two limiting current densities in pH 4 solution at relatively high and low potentials. At pH 12, passivity is observed with a lower limiting current density compared to those observed at pH 4. The corrosion film formed after potentiostatic polarization in the pH 4 solution is composed of a bilayer at a less negative potential and a single layer at a more negative potential. In the case of pH 12 solution, a protective compact bilayer film is formed irrespective of the potential within the passive zone. Overall, the corrosion mechanism of MgZn$_2$ is by early dissolution of Mg leading to a Zn-enriched surface whose subsequent dissolution depends on the value of the applied potential.

**Keywords** MgZn$_2$ · Intermetallic compound · Corrosion · EIS · XPS · FIB-TEM

## Introduction

The 7xxx series Al alloys are widely used in the aerospace and automotive industries, where some properties such as lightweight and high specific strength are very critical requirements. In these alloys, inter-granular corrosion has always been linked to the dissolution of intermetallic phases such as MgZn$_2$ which appear along grain boundaries [1–4]. The MgZn$_2$ is an important hardening phase in 7xxx series Al alloys and in particular 7005 Al alloy [5, 6].

Studies to date indicate that MgZn$_2$ is anodically active relative to the Al alloy matrix [7]. Reports by Ramgopal et al. indicate that MgZn$_2$ is very active with a corrosion potential of − 1.40 V vs. SCE in neutral 0.5 M NaCl solution. Yoon and Buchheit reported a corrosion potential of − 1.24 V vs. SCE for a compositional analog of MgZn$_2$ in neutral 0.1 M NaCl solution. The breakdown potential of MgZn$_2$ was attributed to the onset of Zn dissolution by these authors [5, 6]. These studies reveal that both thermodynamic and kinetic factors are indispensable when considering the corrosion behavior of MgZn$_2$. Other researchers focused on specific areas such as recent works by Diler et al. [8, 9] on the corrosion products on MgZn$_2$ exposed to humid air in the presence and absence of NaCl for 4 and 30 days. These investigations revealed that corrosion of MgZn$_2$ brings about the segregation of Mg at the surface to mainly form Mg hydroxyl carbonates which lead to a passive surface. In the inner layers, metallic Zn was reported to coexist with Mg oxide and hydrozincite. However, these investigations were carried out under neutral conditions; thus, there is limited information on the film forming process at pH values away from the neutral region.

✉ Bo Zhang
bxz011@imr.ac.cn

1    Shenyang National Laboratory for Materials Science, Institute of Metal Research, Chinese Academy of Sciences, 72 Wenhua Rd, Shenyang 110016, China

2    CAS Key Laboratory of Nuclear Materials and Safety Assessment, Institute of Metal Research, Chinese Academy of Sciences, Shenyang 110016, China

3    University of Chinese Academy of Sciences (UCAS), 19A Yuquan Road, Shijingshan District, Beijing 100049, China

4    Department of Pure and Applied Chemistry, University of Calabar, PMB 1115, Calabar, Nigeria

5    CRRC Qingdao Sifang CO., LTD, Qingdao 266111, China

The environmental pH is indeed important, considering the fact that the behavior of anodically polarized Mg and Mg alloys appears not to follow the conventional electrochemical theory. This is due to the phenomenon of "negative difference effect" (NDE) which is capable of causing local alkalization [10, 11]. It is well known that Mg forms a protective film under alkaline conditions. On the other hand, Zn forms an unstable film under alkaline conditions but forms a pseudo-passive film under near-neutral conditions [12, 13]. Obviously, some questions remain regarding the corrosion mechanism of $MgZn_2$ under acidic or alkaline conditions. An investigation over a pH range can allow for a better understanding and prediction of the role of $MgZn_2$ in 7xxx series Al alloys corrosion susceptibility [14, 15]. Studies by Birbilis et al. [2] on the electrochemical characteristics of bulk intermetallic phases in Al alloys using the microcell method disclosed that the electrochemical behavior of intermetallics is more complicated than the simple noble or active classification based on corrosion potential or evaluated from the intermetallic composition.

$MgZn_2$ is present in high number density in 7xxx series Al alloys; this has been observed by TEM (diameter ∼ 10 nm) along the grain boundaries of the alloy matrix [16, 17]. The nanometer-ranged size of $MgZn_2$ has limited the use of conventional electrochemical and microelectrochemical testing methods which require a larger surface area for experiments [18]. In addition to the use of the microelectrochemical testing methods in investigating the intermetallic phases present in an alloy, other options are to produce thin film analogs by flash evaporation [5, 6] or to synthesize the bulk $MgZn_2$ intermetallic compound using information provided in equilibrium diagrams [19]. Bulk synthesis allows for a more elaborate electrochemical and surface product characterization because of the increased sample size.

Acquisition of information on the initial corrosion films increases experimental requirements because the film can be very thin and easily damaged. This calls for sensitive analytical techniques such as the X-ray photoelectron spectroscopy (XPS) and focused ion beam-transmission electron microscopy (FIB-TEM). XPS provides good sensitivity that permits the qualitative and quantitative analysis of corrosion films [20, 21] while the FIB-TEM provides a good local spatial resolution of the corrosion film [22, 23]. In the FIB-TEM technique, an area of interest on the corroded surface is usually coated with Pt or Au. This area of the sample is then cut out using a focused ion beam such that the corrosion film is sandwiched between the coating and the matrix. The cutout TEM lamella is then milled to a dimension that can enable the direct transmission of electrons. Using the TEM lamella, information such as the TEM image and energy dispersive X-ray

(EDX) spectrum as well as the selected area electron diffraction pattern (SAED pattern) can be acquired. FIB in combination with other techniques like glow discharge spectrometry (GDS), TEM, and XPS has been successfully employed in the study of corrosion films [22–25].

The aim of this paper is to improve our understanding of the electrochemical behavior of a bulk-synthesized $MgZn_2$ as a function of pH in an aerated 0.1 M NaCl environment. To clarify certain aspects of the film formation process, XPS was carried out on the film formed in pH 4 and pH 12 solutions while TEM was conducted on the FIB-prepared lamellae of the corrosion film formed in pH 4 solutions.

## Experimental

### Electrochemical tests

The bulk-synthesized $MgZn_2$ intermetallic phase was manufactured by China Material Technology Co. Ltd as described in our previous report [26]. The bulk form of $MgZn_2$ was produced by the combination of commercially pure Mg (99.99%) and pure Zn (99.99%) in the atomic ratio of 1:2 which were then melted in a furnace under vacuum conditions. The melt was cast into a mold, heat treated, and thereafter machined into cylindrical ingots with a diameter of 1 cm. The details of the synthesis of the as-received $MgZn_2$ ingots were sourced from the equilibrium phase diagram. The elemental composition given by energy dispersive X-ray spectroscopy (EDX) analysis revealed that the atomic percentages of Mg and Zn are 33.2% and 66.8%, respectively. This indicates that the Mg/Zn atomic ratio is 1:2 as expected with the molecular formula of $MgZn_2$.

The bulk-synthesized $MgZn_2$ were mounted in contact with epoxy resin with an exposed surface area of about 0.50 $cm^2$. The sample surfaces were then ground down to 3000 grit with silicon carbide papers, cleaned with ethanol, dried in warm air, and immediately taken for electrochemical tests. The solutions were prepared using analytical grade chemicals and distilled water. Electrochemical measurements were carried out in a corrosion cell containing 300 mL of test solution. The setup consisted of a three-electrode system with $MgZn_2$ as a working electrode, platinum (Pt) plate as a counter electrode, and the saturated calomel electrode (SCE) as a reference electrode [27]. All electrochemical measurements were carried out in 0.1 M NaCl solution in an aerated environment at an ambient temperature of (21 ± 2 °C). The pH adjustments of the test solutions were done using acid and alkali to desired values of 2, 4, 6, 10, and 12. The exposed edges of the sample surface were coated with silicone to prevent the occurrence

of crevice corrosion between the electrode and the epoxy mount [28]. All electrochemical experiments were carried out using a PARSTAT 4000 potentiostat.

Anodic potentiodynamic polarization tests were carried out at a scan rate of 0.5 mV/s after monitoring the open circuit potential (OCP) for 10 min. Potentiostatic polarization tests were carried out on another set of freshly prepared $MgZn_2$ electrodes in pH 4 (− 1.10 V vs. SCE and − 1.23 V vs. SCE) and pH 12 (− 1.10 V vs. SCE) solutions. After potentiostatic tests, EIS measurements were taken at 7 points per decade within a frequency range of $10^5$ Hz to $10^{-2}$ Hz and with an amplitude perturbing signal of 5 mV [29]. The fitting of the impedance data was done using the ZSimpWin software. To ensure the reducibility of the results, all electrochemical measurements were taken repeatedly. The potentiostatic and EIS tests were carried out to ascertain the influence of the applied potential in the nature of the corrosion film.

## Corrosion film characterization

XPS analysis was carried out in order to ascertain the chemical composition of the corrosion films after potentiostatic tests in pH 4 and 12 solutions. XPS was carried out using the ESCALAB 250 (Thermo VG) with an X-ray source corresponding to the $K$ peak (1486.6 eV) of Al. The spectrometer power was 150 W with a step size of 0.1 eV and a pass energy of 50.0 eV. The depth profile of the corrosion films was done by sputtering with $Ar^+$ with an energy of 2 kV and a current of 2 A. The XPS data were analyzed with XPSPEAK 4.1 software.

In order to confirm the chemical composition of the films at different potentials, the film corroded in pH 4 solution was analyzed by FIB-TEM. The JOEL (JEM-2100 F) TEM microscope equipped with an EDX detector system was used. The acceleration voltage was 200 kV and the spot size of the beam was 1.2 nm. The TEM lamellae were prepared by a cryo-FIB milling system with Ga ion sputtering. A layer of tungsten was sputtered on an area of interest on the platinum-coated surface of the corroded $MgZn_2$ specimen. The FIB lift-out method was used to extract a cross-sectional lamella of the corroded $MgZn_2$ surface. This lamella was used for the TEM-EDX/SAED analysis [23]. The EDX line scans and SAED patterns were then acquired to determine the elemental profile and the chemical composition of the corrosion films. The SAED patterns were analyzed using the Gatan digital micrograph and Jade XRD pattern processing software. All measured lattice spacing values, $d$, were referenced to the inorganic crystal structure diffraction (ICSD) pattern crystallographic database [22].

# Result

## Potentiodynamic polarization

The anodic potentiodynamic polarization curves of $MgZn_2$ at different pH values in 0.1 M NaCl solutions are shown in Fig. 1. Active anodic dissolution is observed at pH 2 with a relatively high corrosion current density. A lower dissolution rate is observed at pH 4 with two passive regions. These regions are seen between $\sim − 1.20$ and − 1.25 V vs. SCE and between − 1.00 and − 1.15 V vs. SCE with limiting current densities of about $\sim 10$ μA/$cm^2$ and 40 μA/$cm^2$, respectively. In this context, the term passivity is used to rather loosely describe the similar to the noble behavior of $MgZn_2$ under conditions where thermodynamics predicts rapid dissolution [30]. The final breakdown potential is seen at about − 1.00 V vs. SCE after which the trans-passive region prevailed. At pH 6, a lower anodic activity is seen compared to that at pH 4. At pH 10, a passive region is observed between − 1.00 and − 1.15 V vs. SCE and the anodic activity is lower than that observed at lower pH values. At pH 12, a defined passive region is seen between − 0.90 and − 1.20 V vs. SCE with a comparatively low limiting current of $\sim 5$ μA/$cm^2$ and a breakdown potential of − 0.90 V vs. SCE. Overall, the anodic activity of $MgZn_2$ decreases with an increase in pH value from pH 2 to pH 12. This suggests that the stability of the corrosion products formed increases with an increase in the pH [26].

Based on the E-pH diagram of Mg-$H_2O$ and Zn-$H_2O$ system, both Mg and Zn would exhibit active dissolution in the pH 4 solution [30]; however, distinct limiting current densities are seen at pH 4 during potentiodynamic polarization test (Fig. 1). In order to confirm the unexpected results, further electrochemical tests
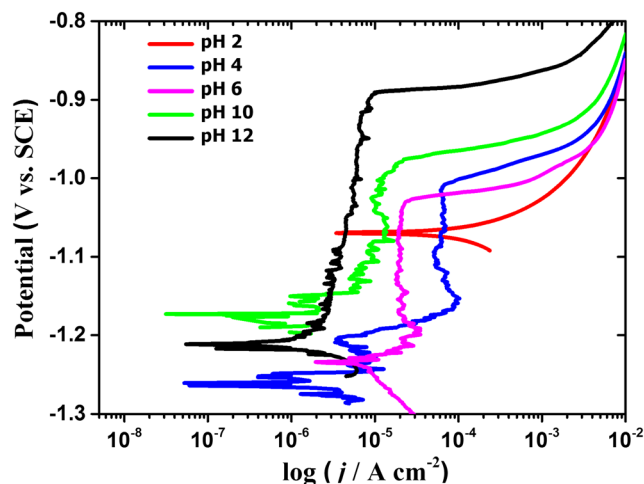


**Fig. 1** Potentiodynamic polarization curves of $MgZn_2$ in aerated 0.1 M NaCl solution at pH 2, 4, 6, 10, and 12 (scan rate, 0.5 mV/s)

(potentiostatic polarization and EIS) were carried out on $MgZn_2$ in pH 4 and pH 12 (for comparison) solutions. Also, the pH after the potentiostatic tests was recorded to find out the possible contribution of pH change to the observed phenomena.

## Potentiostatic polarization

The potentiostatic current transients of $MgZn_2$ in 0.1 M NaCl solution at pH 4 (− 1.10 V vs. SCE and − 1.23 V vs. SCE) and pH 12 (− 1.23 V vs. SCE) are shown in Fig. 2. The current transients are seen not vary significantly with time. The average values recorded at pH 4 (− 1.10 V vs. SCE) and pH 4 (− 1.23 V vs. SCE) are ~ 40 $\mu A/cm^2$ and ~ 10 $\mu A/cm^2$, respectively. This indicates that the anodic dissolution rate of $MgZn_2$ is higher at − 1.10 V vs. SCE compared to − 1.23 V vs. SCE. At pH 12, potentiostatic polarization was carried out only at − 1.10 V vs. SCE and a steady current of ~ 5 $\mu A/cm^2$ was recorded. These indicate that the anodic dissolution rate is greatly reduced in pH 12 solution compared with that of pH 4. The relatively low current density seen at pH 12 solution may be attributed to the formation of a stable protective film on $MgZn_2$. Overall, the magnitude of the current density is in the order: pH 4 (− 1.10 V vs. SCE) > pH 4 (− 1.23 V vs. SCE) > pH 12 (− 1.10 V vs. SCE).

The pH recorded after potentiostatic polarization at pH 4 (− 1.10 V vs. SCE) and pH 4 (− 1.23 V vs. SCE) are 8.2 and 8.6, respectively. In pH 12 solution, the pH after the potentiostatic test is 11.8 and is considered not to change significantly. Obviously, this pH increase at pH 4 is expected to have a great influence on the stability of corrosion products and this is elaborated in the "Discussion" section.
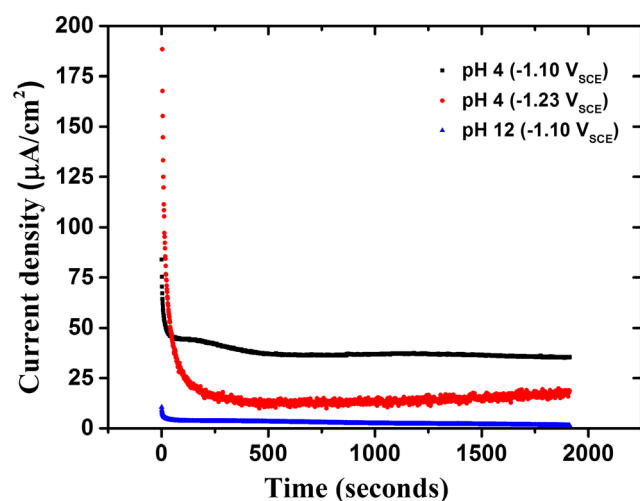


**Fig. 2** Potentiostatic current transients of $MgZn_2$ in 0.1 M NaCl solution at pH 4 (− 1.10 V vs. SCE and − 1.23 V vs. SCE) and pH 12 (− 1.23 V vs. SCE)

## XPS analysis of the corrosion film formed on MgZn₂

XPS analysis was carried out in order to determine the chemical composition of the corrosion films formed after potentiostatic polarization in pH 4 and pH 12 solutions. All binding energies were corrected according to the adventitious C 1s signal (284.6 eV). The spectral lines were deconvolved for the binding energies of O 1s, Mg 1s, and Zn $2p_{3/2}$.

### O 1s data

The high-resolution O 1s spectra at different sputtering times obtained for the corrosion film formed on $MgZn_2$ after potentiostatic polarization at pH 4 and pH 12 are shown in Fig. 3. The sputtering time is directly proportional to the sputtering depth from the film surface into the film. The asymmetric spectra indicate the presence of different compounds of oxygen in the corrosion film. The spectral peaks at 531.0 eV, 532.8 eV, and 530.2 eV correspond to Mg–O, Mg–OH, and Zn–O bonds, respectively.

Figure 3a gives the O 1s spectra at pH 4 (− 1.10 V vs. SCE) after sputtering for 30 s. Peaks corresponding to MgO/$Mg(OH)_2$ are detected and are also present all across the film thickness. However, the intensity of $Mg(OH)_2$ is higher than that of MgO at the near surface and decreases with sputtering time. This suggests that the outermost part of the corrosion film is dominated by $Mg(OH)_2$. Similar observations were made by Wang et al. after potentiostatic polarization of two magnesium alloys, AZ31 and AZ91, at − 1.30 V vs. SCE and − 1.50 V vs. SCE [31]. $Mg(OH)_2$ dominated the film/solution interface due to the very high probability of hydration of MgO [24, 25]. With continuous sputtering into the film formed at pH 4 (− 1.10 V vs. SCE), an additional peak (530.2 eV) corresponding to ZnO is detected in the inner layer after sputtering for 180 s (Fig. 3d). This mixture of Mg and Zn compounds in the inner layer at − 1.10 V vs. SCE indicates that the initial preferential dissolution of Mg is succeeded by Zn oxidation. It can be inferred that the corrosion film is stratified into a bilayer comprising of an outer layer dominated by Mg compounds and an inner layer dominated by Mg/Zn compounds. It has been reported elsewhere that the main corrosion product of Zn in the dilute aqueous solution of NaCl is ZnO [13, 32]. The formation of similar multiple layers of corrosion products by Mg alloys has been reported by Yao et al. and Santamaria et al. [33, 34].

Figure 3b shows the O 1s spectra at pH 4 (− 1.23 V vs. SCE) after 30 s of sputtering. MgO/$Mg(OH)_2$ were detected, and with the progress of sputtering into the inner layers of the film, no additional spectral peak is seen for ZnO compounds. This suggests the enrichment of un-oxidized Zn on the matrix/film interface. The relative intensity of the $Mg(OH)_2$ signal also decreased while that of MgO increased with increase in sputtering time up to 180 s (Fig. 3e).
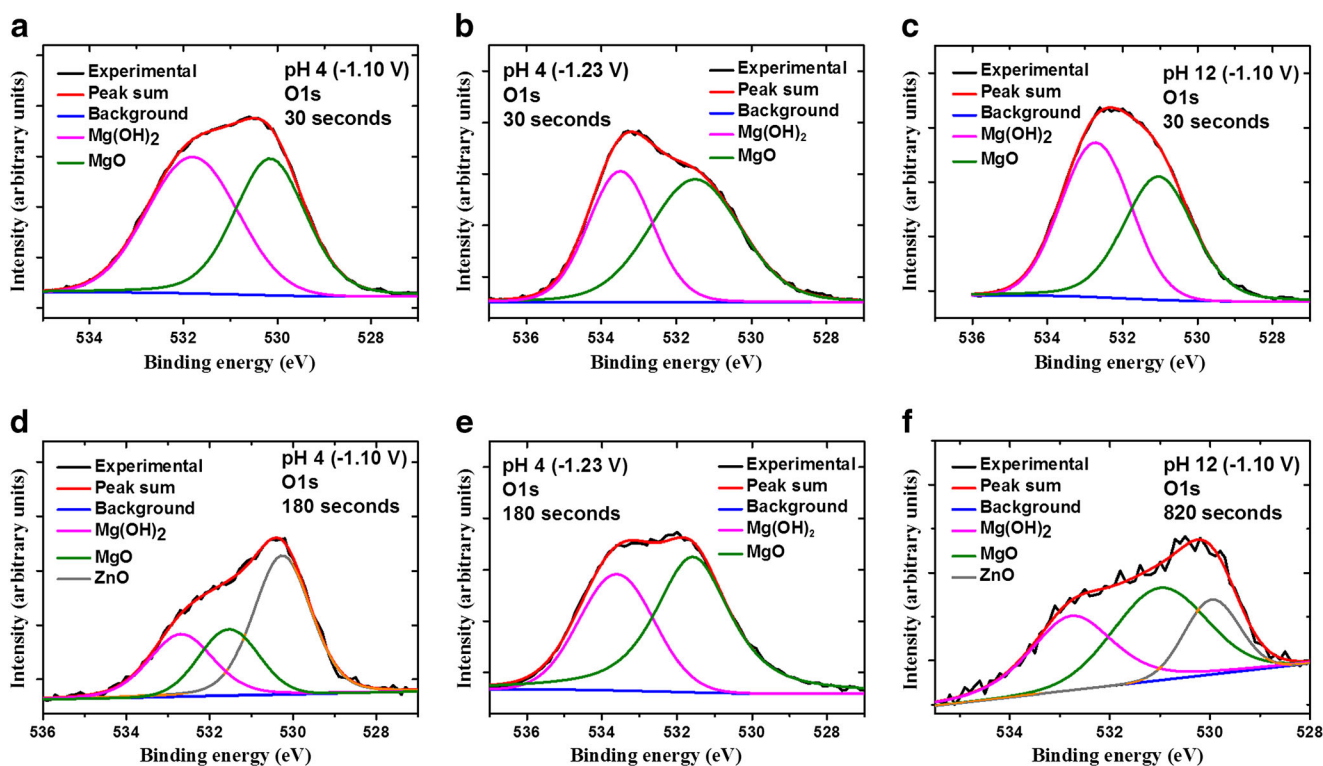
**Fig. 3** XPS deconvolved spectra of O 1s at different sputtering times for the corrosion film formed on MgZn$_2$ after potentiostatic polarization at **a, d** pH 4 (− 1.10 V vs. SCE); **b, e** pH 4 (− 1.23 V vs. SCE); and **c, f** pH 12 (− 1.10 V vs. SCE) solutions

Figure 3c gives the O 1s spectra at pH 12 (− 1.10 V vs. SCE); the results obtained are similar to those at pH 4 (− 1.10 V vs. SCE). The presence of MgO/Mg(OH)$_2$ is detected all across the film and the inner layer was also dominated by Mg/Zn compounds (Fig. 3f). In contrast to the film at pH 4, ZnO was detected at a greater depth after 820 s of sputtering indicating a thicker outer layer of Mg compounds. These results suggest that the corrosion film at pH 12 also consists of a bilayer comprising of a compact outer layer of mainly MgO/Mg(OH)$_2$ and an inner mixture layer of mainly MgO/Mg(OH)$_2$/ZnO.

## Mg 1s data

The presence of MgO and Mg(OH)$_2$ in the corrosion film was confirmed by analyzing the Mg 1s data. The Mg 1s high-resolution spectra after 30 s of sputtering for the corrosion film on MgZn$_2$ after potentiostatic polarization in pH 4 and pH 12 solutions are shown in Fig. 4a–c. The slightly asymmetric curve indicates the presence of different compounds. The peaks at 1302.7 eV and 1303.9 eV correspond to Mg–OH and Mg–O bonds, respectively. Similar analyses were carried out for other sputtering times and peaks corresponding to MgO and Mg(OH)$_2$ were all detected at various depths. The relative intensities of the species are also in line with the results obtained from O 1s data.

## Zn 2p$_{3/2}$ data

The Zn 2p$_{3/2}$ high-resolution binding energy spectra after 180 and 820 s of sputtering for the corrosion film on MgZn$_2$ after potentiostatic polarization in pH 4 and pH 12 solutions are shown in Fig. 4d–f. Metallic Zn enrichment is observed which manifested as a peak at a binding energy corresponding to 1020.9 eV (Fig. 4d–f). At − 1.10 V vs. SCE, the appearance of the peak at 1022.2 eV [28] confirmed the presence of Zn–O bond in the inner layer of the corrosion films at pH 4 and pH 12. The relative intensity of Zn$^0$ is significantly higher than that of ZnO indicating the initial zinc enrichment followed by its dissolution. However, at pH 4 (− 1.23 V vs. SCE), all the Zn are present in the elemental state and no Zn compound is detected (Fig. 4e). The results agree with those obtained for O 1s at pH 4 and 12 (Fig. 3).

The XPS results show that at − 1.23 V vs. SCE, no Zn compound is detected at pH 4 all across the film thickness; instead, elemental Zn enrichment is observed in the inner layer, whereas a bilayer structure is observed at − 1.10 V vs. SCE (pH 4 and 12) which is dominated by an outer layer of MgO/Mg(OH)$_2$ and an inner layer of mainly MgO/Mg(OH)$_2$/ZnO. These results indicate that the nature of the corrosion film depends on pH as well as the applied potential. Diler et al. reported that Mg compounds can migrate towards the surface of the corrosion film with the inner layers being dominated by MgO and metallic Zn when MgZn$_2$ is exposed to humid air.
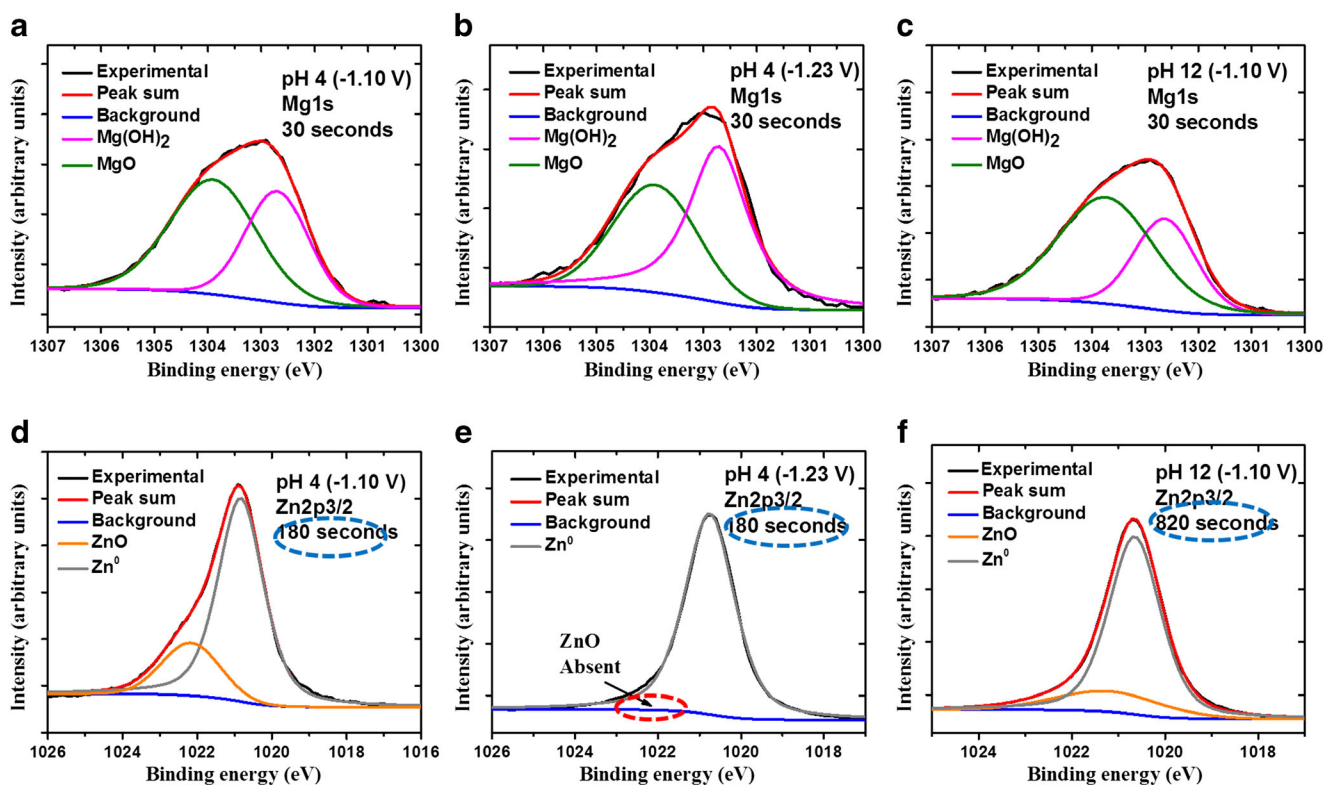
**Fig. 4** XPS deconvolved spectra of **a**–**c** Mg 1s and **d**–**f** Zn 2p for the corrosion film formed on MgZn$_2$ after potentiostatic polarization at pH 4 (− 1.10 V vs. SCE), pH 4 (− 1.23 V vs. SCE), and pH 12 (− 1.10 V vs. SCE) solutions

The observation is linked to the selective dissolution of Mg due to its higher electrochemical activity [9, 19]. Since their study was carried out under open circuit conditions, the absence of Zn compound is consistent with the results observed at relatively lower applied potential in this study.

## FIB/TEM analysis of the corrosion film formed on MgZn$_2$

In order to confirm the elemental distribution and composition of the corrosion films formed at different applied potentials, FIB/TEM was carried out after potentiostatic tests at pH 4 only. The STEM images of the FIB-prepared lamella of the as-cut MgZn$_2$ corroded surface are shown in Fig. 5a and b. The layer of corrosion films formed can be seen sandwiched between platinum and the metal matrix. The film at − 1.10 V vs. SCE is considerably thicker than that at − 1.23 V vs. SCE. A film of about 100 nm is formed on the sample surface at − 1.10 V vs. SCE while that formed at − 1.23 V vs. SCE is just a few tens of nanometers.

### EDX cross-sectional scan

The FIB-prepared lamella was subjected to further analysis in order to get quantitative information on the distribution of elements in the corrosion film section. The EDX scan across

the film formed on the MgZn$_2$ specimen at − 1.10 V vs. SCE and − 1.23 V vs. SCE is presented in Fig. 6. At − 1.10 V vs. SCE, the atomic percentage of O decreased with distance from the outer film towards the sample matrix and that of Zn increased to a steady value within the film while that of Mg dropped and remained fairly constant. It can be seen that the corrosion film is made up of two layers of the different compositions shown by the gray shades (Fig. 6b). At − 1.23 V vs. SCE, the corrosion film is observed to be composed of just a layer of majorly MgO compounds (Fig. 6d).

### TEM-SAED analysis

Additional information on the composition of the corrosion film was obtained using SAED. The selected area for analysis is marked by a circular boundary shown in Fig. 6a and c. The SAED patterns of the corrosion film on MgZn$_2$ after potentiostatic polarization at pH 4 (− 1.10 V vs. SCE) and pH 4 (− 1.23 V vs. SCE) are shown in Fig. 7. Diffraction spots from the corrosion films were identified and the corresponding $r$ values were determined (Table 1). The $d$-spacing was then calculated from the $r$ values and compared with standard ICSD data from which the $hkl$ values were assigned to the corresponding compounds (Fig. 7) [24, 25]. Table 1 shows the determined lattice spacing of
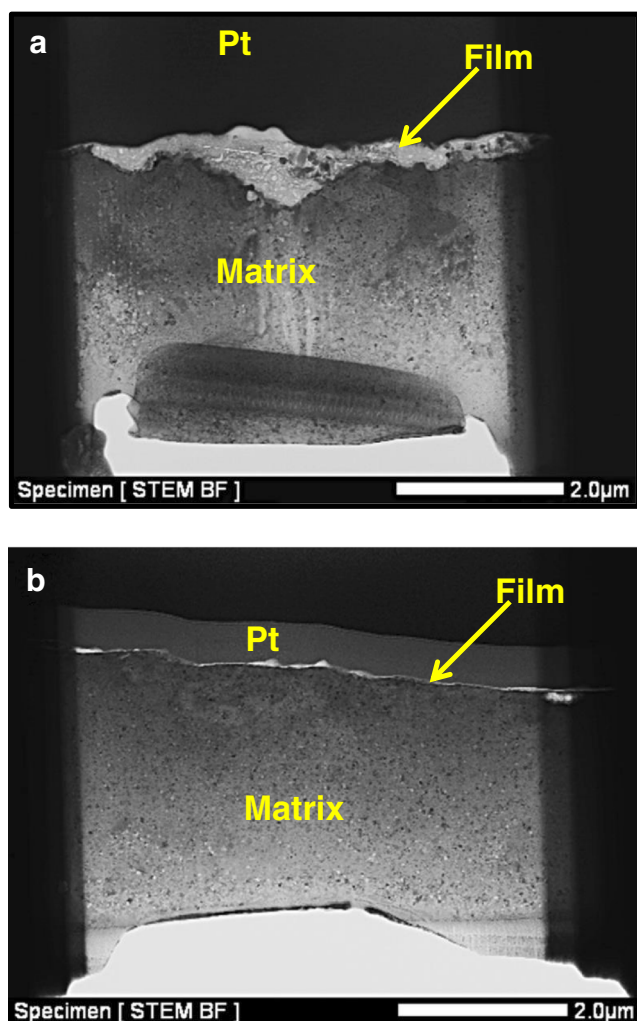
**Fig. 5** STEM images of the focused ion beam (FIB)–prepared sample of MgZn$_2$ specimen after potentiostatic polarization in 0.1 M NaCl at pH 4, **a** − 1.10 V vs. SCE and **b** − 1.23 V vs. SCE

the particles in the corrosion film on MgZn$_2$ and their corresponding *hkl* values. It can be observed in this table that the lattice spacing of the particles in the oxide film matches those of the tabulated compounds in the reference database. The difference between the measured and calculated *d* (nm) for the *hkl* planes is less than ∼ 2%. This is considered to be within acceptable limits for calibrated diffraction patterns of SAED analysis [22].

It is worth mentioning and reiterating that the outer corrosion layer at − 1.10 V vs. SCE is too thin to be selectively mapped out for SAED analysis (Fig. 6b). However, domains within the inner layer at − 1.10 V vs. SCE and the single layer at − 1.23 V vs. SCE were successfully selected for electron diffraction analysis. The compounds identified in the inner part of the bilayer at − 1.10 V vs. SCE are dominated by Mg/Zn compounds while those identified in the single layer at − 1.23 V vs. SCE are dominated by Mg compounds (Fig. 7).

The difference in the surface chemistry of the corrosion film formed on the surface at different potentials which were shown in the XPS analysis (Figs. 3 and 4) was thus validated by FIB/TEM (Figs. 6 and 7).

## EIS analysis

EIS is a very useful and non-destructive technique for the characterization of the stability of the corrosion films [35]. The EIS results after potentiostatic polarization at pH 4 and pH 12 in 0.1 M NaCl solution are given by the Nyquist and Bode plots in Fig. 8a and b. The validity of EIS results may not be easily ascertained by mere inspection of the EIS data, especially when the data is distorted by experimental procedures. To check the validity of the EIS data, the Kramers–Kroning (K–K) relationships were applied to the measured data [36, 37]. Any system that meets the a priori conditions of stability, linearity, and causality is expected to satisfy the K–K relationships. The K–K relationship transforms the real component of the impedance into the imaginary component and vice versa, thus enabling the transformed quantities to be compared directly with their corresponding experimental values for the same parameters. Figure 8c shows the K–K transformations of the real and imaginary components of the EIS data. The K–K transformation shows good agreement between the experimental and transformed impedance data for both real and imaginary components; thus, the system under study complies with the linearity, stability, and causality constraints of linear system theory, thereby validating the EIS data.

The Nyquist plots (Fig. 8a) shows depressed semi-circles whose diameters are directly proportional to the corrosion resistance [38]. The diameter at pH 12 is larger than the one at pH 4 implying that MgZn$_2$ is more corrosion resistant at pH 12. Bode plots (Fig. 8b) indicate that the phase angle peak value at pH 12 (− 76°) is higher compared to pH 4 (− 58° at − 1.23 V vs. SCE and − 53° at − 1.10 V vs. SCE). In the Bode modulus plot (Fig. 8b), the module value of impedance in the low-frequency region could be used to evaluate the corrosion resistance qualitatively. In Fig. 8b, the higher values of the impedance at pH 12 compared to that at pH 4 indicate a higher resistance of MgZn$_2$ towards corrosion at pH 12 [30]. A qualitative assessment of Fig. 8a and b shows that the highest corrosion resistance is recorded in pH 12 (− 1.10 V vs. SCE) solution followed by pH 4 (− 1.23 V vs. SCE) then by pH 4 (− 1.10 V vs. SCE).

According to AC circuit theory, an impedance plot obtained for a given electrochemical system can be correlated with one or more equivalent circuits [30, 35]. A quantitative analysis of the data was carried out by fitting the experimental data with the equivalent circuits shown in Fig. 8d. The equivalent circuit (I) is used to model the corrosion behavior at pH 4 (− 1.23 V vs. SCE) in which a

**Fig. 6** STEM image showing the locations of the analyses and EDX cross-sectional line scan of the corrosion film on $MgZn_2$ surface after potentiostatic polarization at **a, b** − 1.10 V vs. SCE and **c, d** − 1.23 V vs. SCE
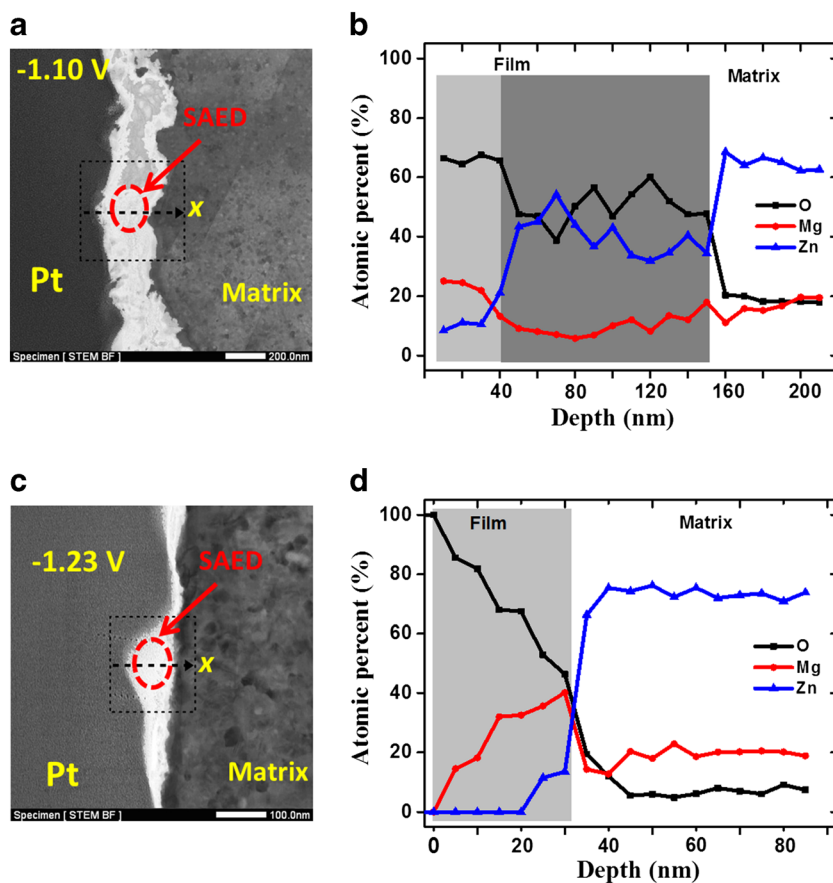
single layer of corrosion film is formed. The equivalent circuit (II) is adopted in order to accommodate the bilayered film formed at pH 4 (− 1.10 V vs. SCE) and pH 12 (− 1.10 V vs. SCE). The components of the circuit are $R_s$, $Q_{dl}$, $R_{ct}$, $Q_1$, $R_1$, $Q_2$, and $R_2$ which represent the resistance of the solution, the capacitance of the double layer, charge transfer resistance, the capacitance of the outer corrosion film, the resistance of the outer corrosion film, the capacitance of the inner corrosion film, and the resistance of the inner corrosion film, respectively. A constant phase element (CPE) denoted by $Q$ in the equivalent circuit is used to represent the behavior of a nonideal capacitor [39–41]. CPE has to do with the distribution of surface roughness, and heterogeneity, electrode porosity, slow adsorption reactions, non-uniform potential, and current distribution. The impedance of the CPE is given by Eq. (1).

$$Z_{CPE} = [Q(j\omega)^n]^{-1} \tag{1}$$

where $Z_{CPE}$ is the relevant impedance, $Q$ is the CPE constant ($\Omega^{-1}$ cm$^{-2}$ s$^n$), $j^2 = -1$, $\omega$ is the circular frequency, and $n$ is the CPE exponent which characterizes deviation of the system from the ideal capacitive behavior The value of $n$ is such that $0 \leq n \leq 1$, when $n = 1$, the CPE can be identified as a capacitance [42–45].

The optimum EIS parameters obtained after fitting the measured values with the equivalent circuit model are illustrated in Table 2. The measured curves are in good agreement with the calculated curves. The standard deviation $X$-squared value is of the order $10^{-4}$. The constant phase element is seen to vary; generally, the lower the constant phase element, the more compact the corrosion film. The electric double layer at a metal surface does not generally behave as a pure capacitance, but rather it behaves as an impedance displaying a frequency-independent phase angle. The effective capacitance $C_{eff}$ can be calculated from the constant phase element using Brug's formula [44, 46–49] given in Eq. (2).

$$C_{eff} = Q^{1/n} \left( \frac{R_s R_{ct}}{R_s + R_{ct}} \right)^{(1-n)/n} \tag{2}$$

The $C_{eff}$ values obtained at pH 4 (− 1.10 V vs. SCE), pH 4 (− 1.23 V vs. SCE), and pH 12 (− 1.10 V vs. SCE) are 27.3 μF/cm$^2$, 13.7 μF/cm$^2$, and 11.7 μF/cm$^2$, respectively. This shows that the order compactness of the corrosion films in the different solutions is pH 12 (− 1.10 V vs. SCE) > pH 4 (− 1.23 V vs. SCE) > pH 4 (− 1.10 V vs. SCE). This is in line with the formation of stable corrosion products by Mg in the alkaline regime.

**Fig. 7** SAED patterns of the corrosion film on MgZn$_2$ after potentiostatic polarization at **a** − 1.10 V vs. SCE and **b** − 1.23 V vs. SCE
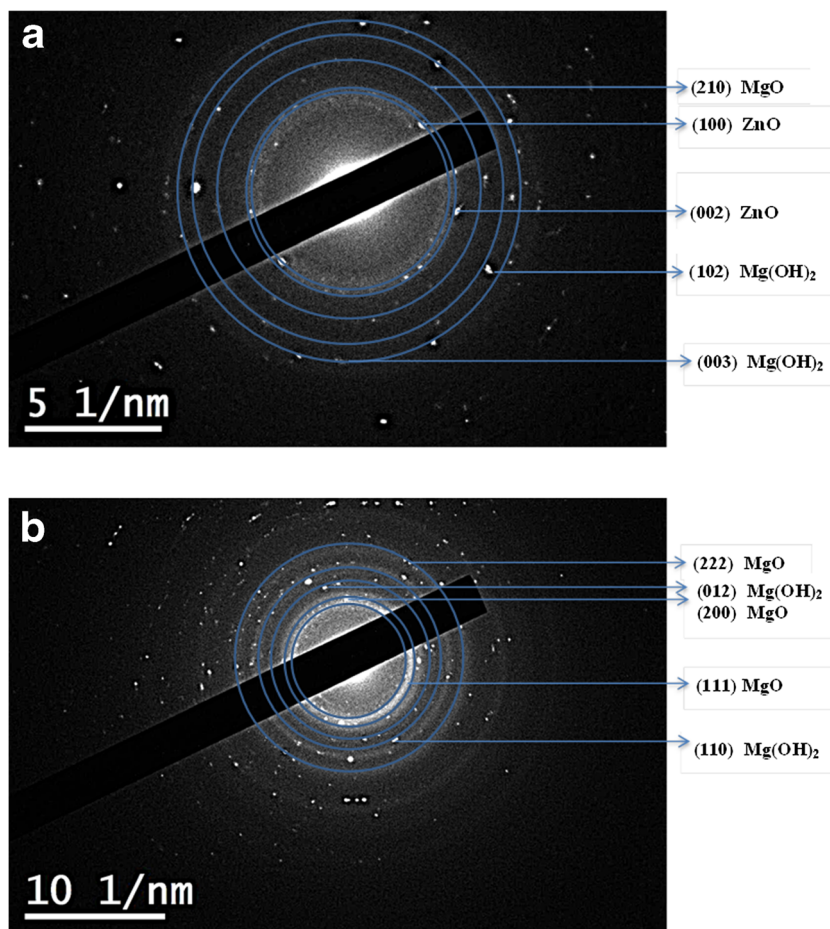


The value of $n$ may be linked to the surface roughness, inhomogeneous reaction rates, and heterogeneous current distribution [32]. The closer the value of $n$ is to 1, the closer the behavior of $Q$ is to that of an ideal capacitor. The lower the values of $Q$, the more compact the corrosion film. The $Q_1$ and $Q_2$ values at pH 12 (− 1.10 V vs. SCE) are less than the values at pH 4 (− 1.10 V vs. SCE); this indicates that a more compact film is formed at pH 12 compared to pH 4 at similarly applied potentials. However, the $Q_1$ values at pH 4 (− 1.23 V vs. SCE) are less than those at pH 4 (− 1.10 V vs. SCE), indicating that a more compact film is formed at − 1.23 V vs. SCE in pH 4 solution.

Table 2 shows that $R_1$ and $R_2$ are larger at pH 12 compared to those at pH 4; this indicates increased corrosion resistance due to the stable corrosion film is formed in the alkaline region [28, 32]. The EIS results show that the highest polarization resistance ($R_{ct} + R_1 + R_2$) is recorded at pH 12 (− 1.10 V vs. SCE) followed by pH 4 (− 1.23 V vs. SCE) and then pH 4 (− 1.10 V vs. SCE). This trend is consistent with the polarization tests (Figs. 1 and 2) in which the order of current density evolved is pH 4 (− 1.10 V vs. SCE) > pH 4 (− 1.23 V vs. SCE) > pH 12 (− 1.10 V vs. SCE).

## Discussion

The results show that the electrochemical behavior of MgZn$_2$ greatly depends on pH as well as applied potential in aqueous solutions. Active dissolution of MgZn$_2$ occurs at pH 2 and the anodic activity decreases with the increase in pH from 2 to 12 (Fig. 1). The corrosion potential of MgZn$_2$ in 0.1 M NaCl is between − 1.07 V vs. SCE and − 1.28 V vs. SCE across the pH range studied which is within the range reported in the literature [5, 6]. Considering the standard electrode potential of Mg and Zn which is − 2.37 V vs. SHE and − 0.76 V vs. SHE, respectively, Mg would preferentially dissolve when present with Zn in a solution [50]. Thus, when MgZn$_2$ is exposed to an aqueous solution, Mg dissolves preferentially as expressed in Eq. (3). This dissolution is usually accompanied by the evolution of hydrogen gas (Eq. (4)) in acidic media [51–54].

$$Mg \rightarrow Mg^{2+} + 2e^- \qquad (3)$$

$$2H^+ + 2e^- \rightarrow H_2 \qquad (4)$$

From thermodynamic predictions and Pourbaix diagrams, no stable film is expected to be formed by Mg with pH < 10.5 although stable Zn compounds may be formed in near neutral solutions. However, at pH 4, MgZn$_2$ behaves as though the

**Table 1** Determined lattice spacing, $d$ (nm), of the nanocrystalline particles in the corrosion film formed on MgZn$_2$ at pH 4

| Potential | $hkl$ | Compound | Measured $d$ (nm) | Calculated $d$ (nm) ICSD |
|---|---|---|---|---|
| − 1.10 V vs. SCE | 100 | ZnO | 0.28 | 0.28 |
| | 002 | ZnO | 0.26 | 0.26 |
| | 210 | MgO | 0.20 | 0.21 |
| | 102 | Mg(OH)$_2$ | 0.18 | 0.18 |
| | 003 | Mg(OH)$_2$ | 0.16 | 0.16 |
| − 1.23 V vs. SCE | 111 | MgO | 0.25 | 0.24 |
| | 200 | MgO | 0.20 | 0.21 |
| | 012 | Mg(OH)$_2$ | 0.18 | 0.18 |
| | 110 | Mg(OH)$_2$ | 0.16 | 0.16 |
| | 222 | MgO | 0.12 | 0.12 |

corrosion film is protective even though the precipitated corrosion film is expected not to be thermodynamically stable. The factors that may be responsible for this observation in the pH 4 solution are elaborated below.

Firstly, metallic Zn enrichment is particularly pivotal in understanding the electrochemical behavior of MgZn$_2$, especially in pH 4 solutions where Zn dissolution is limited due to the open circuit potential of MgZn$_2$ which is below the reversible potential of Zn in aqueous solutions. The dissolution of Mg and Zn is only feasible at potentials above their respective corrosion potentials. The corrosion potential of pure Zn and Mg in 0.1 M NaCl solutions has been widely reported to be − 1.05 V vs. SCE and − 1.30 V vs. SCE, respectively [10, 13], while that of MgZn$_2$ is − 1.27 V vs. SCE (Fig. 1). Obviously, the electrochemical response of MgZn$_2$ would be influenced by the electrochemistry of both Mg and Zn. The corrosion potential of Mg is below that of MgZn$_2$; hence, it corrodes freely above the OCP of MgZn$_2$ (Fig. 4f). The equilibrium potential for Zn$^{2+}$/Zn redox couple is greater than that for Mg$^{2+}$/Mg redox couple; therefore, at − 1.23 V vs. SCE, the dissolution of Zn is not thermodynamically favorable. This leads to elemental Zn enrichment and a decrease in the anodic dissolution rate. This phenomenon of enrichment of more noble metals at the surface of Mg alloys after the dissolution of fractions of monolayers has been reported [55, 56]. At potentials slightly above the OCP of MgZn$_2$ (− 1.23 V vs. SCE), metallic Zn-enriched surface is trapped within a window of highly limited activity. Consequently, the anodic activity on MgZn$_2$ decreases and the corrosion rate is suppressed thus the limiting current density seen in Fig. 1. Given that Zn is within its immunity domain at potentials lower than − 1.05 V vs. SCE [13], the surface tends to be inactive with respect to Zn giving rise to corrosion products dominated by MgO/Mg(OH)$_2$ at − 1.23 V vs. SCE (Figs. 3, 4b, and 7b). As the applied potential increases high enough (− 1.10 V vs. SCE), appreciable amounts of Zn begin to dissolve giving rise to a

second layer (dominated by Mg and Zn compounds) beneath the initially formed layer (Figs. 3 and 7a). A higher limiting current density was recorded at − 1.10 V vs. SCE (compared with that at − 1.23 V vs. SCE); this is attributed to the onset of Zn dissolution as its corrosion potential is approached [5, 13]. The consequence of the above is the formation of a bilayer at − 1.10 V vs. SCE and monolayer at − 1.23 V vs. SCE (Fig. 6).

Secondly, the stabilization of corrosion products due to possible alkalization which accompanies the anodic dissolution of Mg under polarization of MgZn$_2$ is also a crucial issue to be considered. The behavior of anodically polarized Mg appears to show anodic hydrogen evolution (AHE) due to a negative difference effect (NDE) which is accompanied by local alkalization consistent with Eq. (5) [57–60].

$$2H_2O + 2e^- \rightarrow 2OH^- + H_2 \qquad (5)$$

The pH of the system at an initial pH of 4 is observed to rise to values between 8.2 and 8.6 after polarization tests. This is in line with recent reports by Williams et al. [11] who provided the visualization of local cathodes propagating on the surface of dissolving Mg undergoing anodic polarization. Similar reports have also been independently authenticated by other research groups [61, 62]. Furthermore, even when the bulk solution pH is as low as 4, pH values which are above 10 have been theoretically calculated and experimentally measured for corroding Mg surfaces [63, 64]. Obviously, significant alkalization occurs very close to the MgZn$_2$ surface in an acidic medium and this alkalization favors the stabilization of corrosion products (Eqs. (6) and (7)) which is demonstrated by XPS results (Fig. 3).

$$Mg^{2+} + OH^- \rightarrow Mg(OH)_2 \qquad (6)$$

$$Mg(OH)_2 \rightarrow MgO + H_2O \qquad (7)$$

At elevated potentials (− 1.10 V vs. SCE), anodic dissolution of Zn proceeds by Eq. (8) and the corrosion products are consistent with Eq. (9). These Zn compounds can bring about
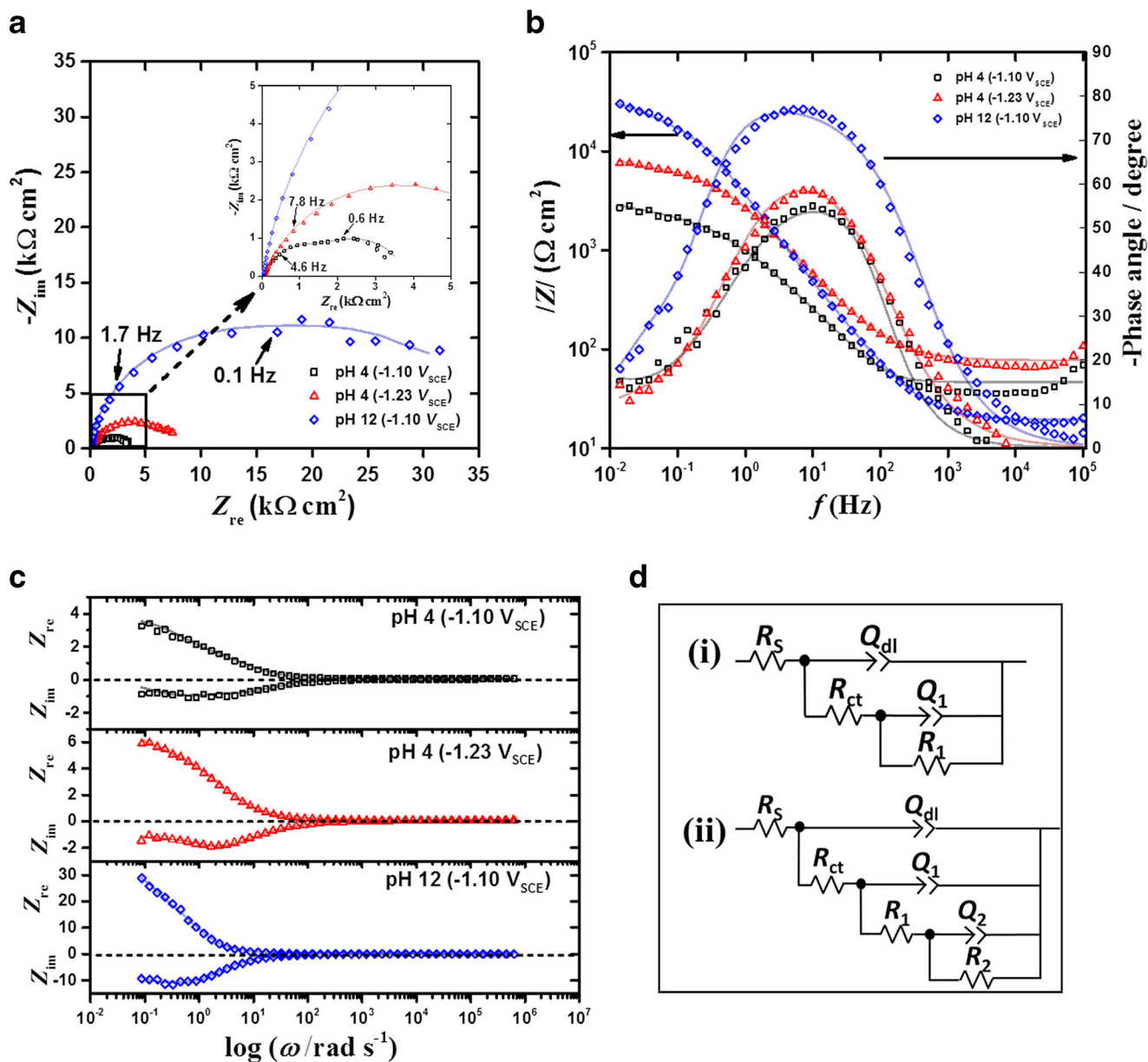
**Fig. 8** Electrochemical impedance response of MgZn$_2$ after potentiostatic polarization in 1.0 M NaCl solution at pH 4 (− 1.10 V vs. SCE and − 1.23 V vs. SCE) and pH 12 (− 1.10 V vs. SCE). **a** Nyquist plot (the frequencies indicated correspond to the frequency of the time constant of the corrosion films), **b** Bode plot (modulus vs. frequency) and Bode plot (phase angle vs. frequency), and **c** K–K transforms of the real ($Z_{re}$ in kΩ cm$^2$) and imaginary ($Z_{im}$ in kΩ cm$^2$) components of the EIS data. The continuous lines represent the fitted data. **d** Impedance equivalent circuit models

volume expansion and growth of the inner film and an increase in the porosity of the film [13, 65].

$$Zn \rightarrow Zn^{2+} + 2e^- \qquad (8)$$

$$Zn^{2+} + 2OH^- \rightarrow ZnO + H_2O \qquad (9)$$
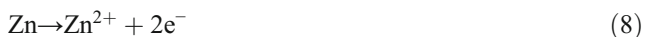
Although ZnO is thermodynamically stable in the near neutral environment, it does not form an effective barrier against corrosion. In the literature, a domain of pseudo-passivity of Zn has been reported to exist between pH 4 and pH 10 solutions [13, 65]. However, even though the corrosion products are expected to be unstable in pH 4 solution, the dissolution kinetics may be slow and a surface corrosion film can still be formed on MgZn$_2$ provided the dissolution kinetics are not faster than the formation kinetics [66].

Nevertheless, it is worth reiterating that the corrosion films formed in pH 4 solutions are not really passive and so do not offer effective protection for MgZn$_2$ especially when compared to the stable film formed at pH 12 which offers greater protection (Fig. 8). In pH 12 solution, corrosion of MgZn$_2$ occurs mainly by the formation of stable MgO/Mg(OH)$_2$ films with ZnO in the inner layers [67].

**Table 2** Optimum EIS parameters obtained for MgZn$_2$ at pH 4 and 12 after potentiostatic polarization in 0.1 M NaCl solution

| System | $R_s$ | $Q_{dl}$ | $n$ | $R_{ct}$ | $Q_1$ | $n_1$ | $R_1$ | $Q_2$ | $n_2$ | $R_2$ |
|---|---|---|---|---|---|---|---|---|---|---|
| pH 4 (− 1.10 V vs. SCE) | 57 | $3.1 \times 10^{-5}$ | 0.98 | $2.0 \times 10^2$ | $1.6 \times 10^{-4}$ | 0.66 | $2.3 \times 10^3$ | $2.2 \times 10^{-3}$ | 0.80 | $7.1 \times 10^2$ |
| pH 4 (− 1.23 V vs. SCE) | 55 | $1.5 \times 10^{-5}$ | 0.99 | $8.7 \times 10^1$ | $2.6 \times 10^{-5}$ | 0.89 | $6.3 \times 10^3$ | – | – | – |
| pH 12 (− 1.10 V vs. SCE) | 45 | $2.7 \times 10^{-5}$ | 0.90 | $1.7 \times 10^1$ | $3.6 \times 10^{-5}$ | 0.90 | $1.7 \times 10^4$ | $3.4 \times 10^{-4}$ | 0.71 | $1.3 \times 10^4$ |

The unit of resistance is $\Omega$ cm$^2$ and the unit of the admittance is $\Omega^{-1}$ cm$^{-2}$ s$^n$

In summary, a comparison of the electrochemical behavior of MgZn$_2$ at pH 4 and 12 (Fig. 4) reveals similar film structures in each of the two solutions at − 1.10 V vs. SCE. In contrast, the outer layer of MgO/Mg(OH)$_2$ at pH 12 is thicker and more compact than that at pH 4 (Figs. 3, 4, and 8) and it is not affected by the applied potential within the passive zone (Fig. 1). Partially stable films manifest at pH 4 while a stable film is observed at pH 12. In alkaline media, solubility factors become more important, thereby promoting the formation of stable MgO/Mg(OH)$_2$ layer. Hence, the corrosion resistance of MgZn$_2$ can be understood based on the stability of Mg corrosion products and metallic Zinc enrichment.

## Conclusions

The following conclusions have been drawn from the obtained results:

1. The electrochemical behavior of MgZn$_2$ depends on pH as well as applied potential. The anodic activity of MgZn$_2$ decreases with an increase in pH value.
2. The corrosion film formed in pH 4 solution at a less negative potential (− 1.10 V vs. SCE) is stratified into a bilayer which comprises of an outer layer dominated by MgO/Mg(OH)$_2$ and an inner layer dominated by MgO/Mg(OH)$_2$/ZnO. The film formed at a lower potential (− 1.23 V vs. SCE) is a single layer dominated by MgO/Mg(OH)$_2$. The film at pH 12 (− 1.10 V vs. SCE) is comprised of a compact bilayer of MgO/Mg(OH)$_2$ outer layer and MgO/Mg(OH)$_2$/ZnO inner layer.
3. EIS results indicate that the corrosion resistance of MgZn$_2$ at pH 12 is significantly higher than that at pH 4 owing to the increased stability of corrosion products in the alkaline region. At pH 4, the corrosion resistance at − 1.23 V vs. SCE is higher than that at − 1.10 V vs. SCE.
4. Generally, the corrosion of MgZn$_2$ in 0.1 M NaCl solution proceeds with the initial preferential dissolution of Mg leading to Zn enrichment whose subsequent dissolution depends on pH and applied potential.

## References

1. Andreatta F, Lohrengel MM, Terryn H, de Wit JHW (2003) Electrochim Acta 48(20–22):3239–3247
2. Birbilis N, Buchheit RG (2005) J Electrochem Soc 152(4):B140–B151
3. Birbilis N, Padgett BN, Buchheit RG (2005) Electrochim Acta 50(16-17):3536–3544
4. Ramgopal T, Gouma PI, Frankel GS (2002) Corrosion 58(8):687–697
5. Ramgopal T, Schmutz P, Frankel GS (2001) J Electrochem Soc 148(9):B348–B356
6. Yoon Y, Buchheit RG (2005) Electrochem Solid St Lett 8(11):B65–B68
7. Wloka J, Virtanen S (2008) Surf Interface Anal 40(8):1219–1225
8. Diler E, Lescop B, Rioual S, Vien GN, Thierry D, Rouvellou B (2014) Corros Sci 79:83–88
9. Diler E, Rioual S, Lescop B, Thierry D, Rouvellou B (2012) Corros Sci 65:178–186
10. Birbilis N, King AD, Thomas S, Frankel GS, Scully JR (2014) Electrochim Acta 132:227–283
11. Williams G, Birbilis N, McMurray HN (2013) Electrochem Commun 36:1–5
12. Alsagabi S, Ninlachart J, Raja KS, Charit I (2016) J Mater Eng Perform 25(6):2364–2374
13. Thomas S, Birbilis N, Venkatraman MS, Cole IS (2012) Corrosion 68:1–9
14. Moon S-M, Pyun S-I (1999) J Solid State Electrochem 3(2):104–110
15. Pyun S-I, Moon S-M (2000) J Solid State Electrochem 4(5):267–272
16. Birbilis N, Cavanaugh MK, Buchheit RG (2006) Corros Sci 48(12):4202–4215
17. Sun XY, Zhang B, Lin HQ, Zhou Y, Sun L, Wang JQ, Han EH, Ke W (2013) Corros Sci 77:103–112
18. Suter T, Alkire RC (2001) J Electrochem Soc 148(1):B36–B42
19. Diler E, Rouvellou B, Rioual S, Lescop B, Vien GN, Thierry D (2014) Corros Sci 87:111–117
20. Fujimoto S, Kim W-S, Sato M, Son J-Y, Machida M, Jung K-T, Tsuchiya H (2015) J Solid State Electrochem 19(12):3521–3531
21. Santamaria M, Di Franco F, Di Quarto F, Pisarek M, Zanna S, Marcus P (2015) J Solid State Electrochem 19(12):3511–3519
22. Ghods P, Isgor OB, Carpenter GJC, Li J, McRae GA, Gu GP (2013) Cement Concrete Res 47:55–68
23. Li J, Malis T, Dionne S (2006) Mater Charact 57(1):64–70
24. Yang J, Yim CD, You BS (2016) J Electrochem Soc 163(8):C395–C401

25. Yang J, Yim CD, You BS (2016) J Electrochem Soc 163(14):C839–C844

26. Ikeuba AI, Zhang B, Wang J, Han E-H, Ke W, Okafor PC (2018) J Electrochem Soc 165(3):C180–C194

27. Scendo M, Staszewska-Samson K (2017) Int J Electrochem Sci 12:5668–5691

28. Shang X-L, Zhang B, Han E-H, Ke W (2011) Electrochim Acta 56(3):1417–1425

29. Valandro LF, Neisser MP, Lopes AG, Scotti R, Andreatta OD, Bottino MA (2003) J Dent Res, vol 82, pp B344–B344

30. Kaesche H (2003) Corrosion of metals. Engineering Materials and Processes. Springer, New York

31. Wang L, Shinohara T, Zhang BP (2010) Appl Surf Sci 256(20):5807–5812

32. Zhang B, Zhou H-B, Han E-H, Ke W (2009) Electrochim Acta 54(26):6598–6608

33. Santamaria M, Di Quarto F, Zanna S, Marcus P (2007) Electrochim Acta 53(3):1314–1324

34. Yao HB, Li Y, Wee ATS (2000) Appl Surf Sci 158(1-2):112–119

35. Bard AJ, Faulkner LR (1980) Electrochemical methods: fundamentals and applications. Wiley, New York

36. Ismail KM, Wood TK, Earthman JC (1999) Electrochim Acta 44(26):4685–4692

37. Zheng ZJ, Gao Y, Gui Y, Zhu M (2014) J Solid State Electrochem 18(8):2201–2210

38. Heakal FE-T, Fatayerji MZ (2010) J Solid State Electrochem 15:125–138

39. Mahovic Poljacek S, Risovic D, Cigula T, Gojo M (2011) J Solid State Electrochem 16:1077–1089

40. Moon S-M, Pyun S II (1998) J Solid State Electrochem 2(3):156–161

41. Zerbino J, Gassa L (2003) J Solid State Electrochem 7(3):177–182

42. Belkaid S, Ladjouzi MA, Hamdani S (2011) J Solid State Electrochem 15(3):525–537

43. Jorcin JB, Orazem ME, Pebere N, Tribollet B (2006) Electrochim Acta 51(8-9):1473–1479

44. Lasia A (2014) Electrochemical impedance spectroscopy and its applications. Springer, New York

45. Pyun S-I, Shin H-C, Lee J-W, Go J-Y (2012) Electrochemistry of insertion materials for hydrogen and lithium. In: Scholz F (ed) Monographs in electrochemistry. Springer, Berlin

46. Brug GJ, Van den Eeden ALG, Sluyters-Rehbach M, Sluyters JH (1984) J Electroanal Chem 176(1-2):275–295

47. Hirschorn B, Orazem ME, Tribollet B, Vivier V, Frateur I, Musiani M (2010) Electrochim Acta 55(21):6218–6227

48. Ma H, Cheng X, Li G, Chen S, Quan Z, Zhao S, Niu L (2000) Corros Sci 42(10):1669–1683

49. Wang W, Alfantazi A (2014) Electrochim Acta 131:79–88

50. Lindsey AJ (1966) Pourbaix, M - Atlas of electrochemical equilibria in aqueous solutions. Chem Ind, London

51. Ghali E (2011) 2 - Activity and passivity of magnesium (Mg) and its alloys A2. In: Song G-L (ed) Corrosion of Magnesium Alloys. Woodhead Publishing, Cambridge

52. Ghali E, Dietzel W, Kainer KU (2004) J Mater Eng Perform 13(1):7–23

53. Ikeuba AI, Okafor PC (2018) Pigm Resin Technol. https://doi.org/10.1108/prt-03-2018-0020

54. Ikeuba AI, Okafor PC, Ekpe UJ, Ebenso EE (2013) Int J Electrochem Sci 8:7455–7467

55. Asmussen RM, Danaie M, Botton GA, Shoesmith DW (2013) Corros Sci 75:114–122

56. Taheri M, Kish JR, Birbilis N, Danaie M, McNally EA, McDermid JR (2014) Electrochim Acta 116:396–403

57. Atrens A, Dietzel W (2007) Adv Eng Mater 9(4):292–297

58. Petty RL, Davidson AW, Kleinberg J (1954) J Am Chem Soc 76(2):363–366

59. Shi Z, Jia JX, Atrens A (2012) Corros Sci 60:296–308

60. Song G, Atrens A, John DS, Wu X, Nairn J (1997) Corros Sci 39(10-11):1981–2004

61. Ralston KD, Williams G, Birbilis N (2012) Corrosion 68(6):507–517

62. Williams G, McMurray HN (2008) J Electrochem Soc 155(7):C340–C349

63. Isaacs HS, Adzic G, Jeffcoate CS (2000) Corrosion 56(10):971–978

64. Shi HW, Tian ZH, Hu TH, Liu FC, Han EH, Taryba M, Lamaka SV (2014) Corros Sci 88:178–186

65. Thomas S, Cole IS, Sridhar M, Birbilis N (2013) Electrochim Acta 97:192–201

66. Zhao M-C, Liu M, Song G-L, Atrens A (2008) Corros Sci 50(11):3168–3178

67. McCafferty E (2010) Thermodynamics of corrosion: Pourbaix diagrams. In: Introduction to corrosion science. Springer, New York. https://doi.org/10.1007/978-1-4419-0455-3_6